Check for updates

Enhancement of NH₃-SCR performance of LDH-based MMnAl (M = Cu, Ni, Co) oxide catalyst: influence of dopant M†

Yali Du,‡[a] Lili Liu,‡[b] Yalin Feng,[b] Baoshuan Yang [ID][b] and Xu Wu [ID] *[b]

Transition metal (Cu, Ni, Co) doped MnAl mixed oxide catalysts were prepared through a novel method involving the calcination of hydrotalcite precursors for the selective catalytic reduction of NO_x with NH_3 (NH_3-SCR). The effects of transition metal modification were confirmed by means of XRD, BET, TEM, XPS, NH_3-TPD, and H_2-TPR measurements. Experimental results evidenced that CoMnAl-LDO presented the highest NO_x removal efficiency of over 80% and a relatively high N_2 selectivity of over 88% in a broad working temperature range (150–300 °C) among all the samples studied. Moreover, the CoMnAl-LDO sample possessed better stability and excellent resistance to H_2O and SO_2. The reasons for such results could be associated with the good dispersion of Co_3O_4 and MnO_x, which could consequently provide optimum redox behavior, plentiful acid sites, and strong NO_x adsorption ability. Furthermore, dynamics calculations verified the meaningful reduction in apparent activation energy (E_a) for the CoMnAl-LDO sample, which is in agreement with the DeNO$_x$ activity.

1. Introduction

Nitric oxide (NO_x), which is mainly generated from stationary and automotive sources, has definitely given rise to many problems for the environment and has resulted in health concerns for humans.[1–3] With gradually tightening regulations on NO_x emission limits, post-treatment of nitrogen oxides has become one of the most important research challenges the world faces today in the environmental domain. Currently, selective catalytic reduction (SCR) has been put into wide commercial utilization to abate NO_x.[4–6] Most practical catalysts in the SCR system are vanadium-based catalysts that must be installed upstream of dedusting and desulfurization to satisfy their optimal operating temperature of 300–400 °C or the catalysts could be poisoned by high concentrations of dust particles and sulfur-containing ammonium salts.[7–9] In this situation, it is necessary to develop low-temperature and environmentally friendly catalysts which can efficiently work in the downstream and avoid those problems mentioned above.

Mn-based DeNO$_x$ catalysts have been extensively explored in the low-temperature NH₃-SCR field due to their unique redox properties, as they are sensitive to H_2O and SO_2.[10,11] To overcome these issues, transition metals have been introduced to Mn-based catalysts to modulate their redox ability and acid sites.[12–14] For example, Qiu successfully designed $Mn_xCo_{3-x}O_4$ nanoparticles through nanocasting, which presented superior catalytic performance to bulk $MnCo_2O_4$ synthesized through the co-precipitation method.[15]

In recent years, calcined layered double hydroxides (LDHs) have shown potential use as catalysts for several reasons, such as the possibility of tuning the composition in wide scope, their high surface areas and homogenous distribution of introduced cations.[16–18] In addition, Al was proved to be of great necessity to enhance the self-stability of the LDH materials. From LDH precursors, Yan et al.[19] prepared $Cu_{0.5}Mg_{1.5}Mn_{0.5}Al_{0.5}O_x$, which presented superior catalytic performance in a wide temperature range compared to Mn/γ-Al_2O_3 prepared by conventional methods. This method might enable good dispersion of the active metal species to provide strong internal interactions for the $Cu_{0.5}Mg_{1.5}Mn_{0.5}Al_{0.5}O_x$ catalyst.

Based on the abovementioned points, using LDHs own innate advantages to accomplish the effective doping of transition metal into MnAl oxides could facilitate DeNO$_x$ performances. Herein, Cu-, Ni- or Co-doped MnAl mixed metal oxide catalysts were investigated for NH₃-SCR at low temperatures, taking into account the characterization results of XRD (X-ray diffraction), BET (Brunauer–Emmett–Teller), XPS (X-ray photoelectron spectroscopy), NH₃-TPD (NH₃-temperature programmed desorption), H_2-TPR (H_2-temperature programmed reduction), NO + O_2-TPD (NO + O_2-temperature programmed desorption), etc. The addition of Co into MnAl oxide is proposed to dramatically increase its catalytic ability and behaviour, as

[a]*College of Chemistry and Chemical Engineering, Jinzhong University, Jinzhong, 030619, PR China. E-mail: dyl0037@163.com*

[b]*College of Chemistry and Chemical Engineering, Taiyuan University of Technology, Taiyuan 030024, PR China. E-mail: wuxu@tyut.edu.cn; Tel: +86-351-6018528*

† Electronic supplementary information (ESI) available. See DOI: 10.1039/c9ra08391j

‡ These authors contributed equally to this work.

CoMnAl-LDO presented preferable DeNO$_x$ activity (over 80% NO conversion) and N$_2$ selectivity in a broad working temperature window (150–300 °C). In addition, the CoMnAl-LDO sample possessed better stability and excellent resistance to H$_2$O and SO$_2$ at 240 °C.

2. Experimental section

2.1 Preparation of MMnAl-LDO (M = Cu, Ni, Co)

The MMnAl-LDH (M = Cu, Ni, and Co) materials were prepared by co-precipitation method. 50% Mn(NO$_3$)$_2$, Al(NO$_3$)$_3$·9H$_2$O and Cu(NO$_3$)$_2$·3H$_2$O (or Ni(NO$_3$)$_2$·6H$_2$O, Co(NO$_3$)$_2$·6H$_2$O) were dissolved in deionized water, in which the molar ratios of M^{2+} to Mn^{2+} and M^{2+} to M^{3+} were 3 : 1 and 4 : 1 (M^{2+}/Mn^{2+} = 3 and M^{2+}/M^{3+} = 4 : 1), respectively. Then, the above aqueous solution was added into 1 mol l^{-1} NaOH solution with vigorous stirring. In order to avoid oxidation of M^{2+}, N$_2$ was injected during the whole aging process. The pH of the solution was kept at 9–10. The resulting slurry was transferred into a reaction vessel for about 6 h at 60 °C. Finally, MMnAl-LDH (M = Cu, Ni, and Co) materials were obtained by drying at 60 °C overnight in an oven. After being calcined at 500 °C for 5 h at a rate of 2 °C min^{-1} in air, diverse mixed metal oxides were prepared which were labelled CuMnAl-LDO, NiMnAl-LDO and CoMnAl-LDO. Meanwhile, the MnAl-LDH and corresponding MnAl-LDO were prepared by a similar method.

2.2 Catalyst characterization

The X-ray diffraction (XRD) patterns for pristine hydrotalcites and corresponding mixed metal oxides were tested with a Rigaku D/max-2500 diffractometer with a Cu/Kα radiation source. The operating range for 2θ was from 5 to 85° and the scanning rate was 8° min^{-1}. FT-IR experiments were carried out on an FTS 3000 MX FT-IR (Bruker Vertex70) spectrophotometer. The morphologies of the obtained hydrotalcites were measured by an SU8010 SEM apparatus with an accelerating voltage of 200 kV. TEM was carried out on a JEM 2100F transmission electron microscope. The TGA was performed on a Q50 TGA analyzer equipped with a quadrupole mass spectrometer (QMS). The range of testing temperature was from room temperature to 900 °C in flowing Ar (80 mL min^{-1}) at the heating rate of 10 °C min^{-1}. The surface areas for hydrotalcite-derived mixed oxides were obtained via the BET method. The operating instrument was a Micromeritics ASAP-2020 which needs −196 °C liquid nitrogen during operation. In addition, the t-plot approach was used to analyze the total pore volume and the pore size distributions were analyzed by BJH (Barrett–Joyner–Halenda) method. H$_2$-TPR was performed in a TP-5080 instrument. A U-shaped quartz reactor is filled with 80 mg catalyst (40–60 mesh). Before operation, the samples were activated at 300 °C for 1 h under Ar flow. Next, the temperature of the catalyst was decreased to room temperature. Then the catalyst was heated to 800 °C with a ramping rate of 10 °C min^{-1} in 5% H$_2$/Ar (30 mL min^{-1}) and data were collected during the process. For NH$_3$-TPD, the amount of catalyst and the initial activation process were the same as H$_2$-

TPR. Next, unlike the H$_2$-TPR, the catalyst was exposed to NH$_3$ at 50 °C for 1 h, followed by removing unstably adsorbed species by blowing He for 30 min. Then, the desorption process of NH$_3$ was performed with the temperature of the reactor rising to 750 °C at a rate of 10 °C min^{-1}. NO + O$_2$-TPD experiments were operated on a fixed bed reactor self-assembled in the laboratory. First, the catalyst was pre-treated at 300 °C under N$_2$ flow for 1 h. Then, adsorption of 5 vol% O$_2$ and 500 ppm NO was implemented at 50 °C for 1 h, followed by physical removal of adsorbed NO$_x$ with N$_2$ for 0.5 h. Finally, the temperature of samples was raised from 50 to 400 °C with an ascending rate of 10 °C min^{-1} under N$_2$ flow. A Thermo Fisher IS10 FTIR was used to record the concentrations of NO$_x$ for the inlet and outlet gases. XPS analysis was carried out on an ESCALab 250 electron spectrometer (Thermo Scientific Corporation) in which the Al Kα radiation source (1486.6 eV) was adopted at 15 kW accelerating power. In order to compensate for the charge effect of catalysts, the C 1s peak of 284.6 eV was used to calibrate all binding energies (BE) of catalysts. The in situ DRIFT spectra were carried out on a Nicolet 6700 instrument produced by the Simefei company and equipped with a liquid nitrogen-cooled MCT detector with 4 cm^{-1} resolution. Before each measurement, the sample was pre-treated under N$_2$ atmosphere for 30 min (300 °C) and then cooled to 50 °C while the background was recorded. Subsequently, 500 ppm NO + 5% vol. O$_2$ was introduced into the cell and the DRIFT spectra were recorded. The final spectra were obtained after NO + O$_2$ co-adsorption for 30 min and purging with N$_2$ for another 10 min.

2.3 Catalytic activity test

The activity testing was performed in fixed-bed reactor. A quartz reactor was filled with 0.3–0.4 g catalysts (40–60 mesh). A model flue gas (500 ppm NH$_3$, 500 ppm NO, 5 vol% O$_2$, 0 or 100 ppm SO$_2$, 0 or 10 vol% H$_2$O, and N$_2$ as equilibrium gas) was used in all experiments. During the process, the flow rate was 187 cm^3 min^{-1} and the gas hourly space velocity (GHSV) was 45 000 h^{-1}. A Thermo Fisher IS10 FTIR was used to record the concentrations of NO$_x$ for the inlet and outlet gases every 10 min in the temperature range of 90–360 °C.

The NO$_x$ conversion and N$_2$ selectivity were separately calculated basing on the following formulas:

$$NO_x \text{ conversion } (\%) = \left\{ \frac{[NO_x]_{in} - [NO_x]_{out}}{[NO_x]_{in}} \right\} \times 100\%$$

N$_2$ selectivity (%)

$$= \left\{ \frac{\{[NO_x]_{in} + [NH_3]_{in} - [NO_x]_{out} - 2[N_2O]_{out} - [NH_3]_{out}\}}{[NO_x]_{in} + [NH_3]_{in} - [NO_x]_{out} - [NH_3]_{out}} \right\}$$
$$\times 100\%$$

where the inlet concentrations of NO, NO$_2$ and NH$_3$ were labelled [NO]$_{in}$, [NO$_2$]$_{in}$ and [NH$_3$]$_{in}$, respectively, and the outlet concentrations of NO, NO$_2$ and N$_2$O were labelled [NO]$_{out}$, [NO$_2$]$_{out}$ and [N$_2$O]$_{out}$, respectively.

2.4 Kinetic test

The feed-gas mixture is the same as in the above activity test. In order to eliminate the diffusion effect, experiments were performed with different particle sizes and different flow rates. For the NH_3-SCR model reaction, the apparent activation energies (E_a) for these catalysts were acquired from the following formula:

$$\ln k = -\frac{E_a}{RT} + \ln A$$

where the reaction rate constant ($cm^3\ g^{-1}\ s^{-1}$), the pre-exponential factor ($cm^3\ g^{-1}\ s^{-1}$), the standard gas constant ($J\ mol^{-1}\ K^{-1}$), and the reaction temperature (K) were respectively labelled as k, A, R, and T.

The reaction rate constant (k) as a function of NO conversion (%) can be calculated through the formula below:

$$k = -\frac{V}{W} \times \ln(1-x)$$

in which the reaction rate coefficient ($cm^3\ g^{-1}\ s^{-1}$), the catalyst weight (g), the volumetric flow rate ($cm^3\ s^{-1}$) and the NO conversion (%) were labelled as k, W, V and x, respectively.

3. Results and discussion

3.1 The structure characterization of catalysts

3.1.1 XRD analysis of pristine LDHs. XRD was used to investigate the crystalline micro-structures of the initial LDH precursors, as displayed in Fig. 1. All the prepared samples displayed distinctive diffraction peaks for the (003) and (006) planes characteristic of hydrotalcites.[20] It is worth mentioning that the transition metal (Cu, Ni or Co) incorporation did cause distinct modification of the precursors in which their FWHM became significantly wider. Considering the Scherrer formula, this conveyed that the three doped precursors possessed relatively smaller crystal sizes. This phenomenon hinted that the transition metal (Cu, Ni or Co) doping changed the morphology of LDHs precursors, which should contribute to the
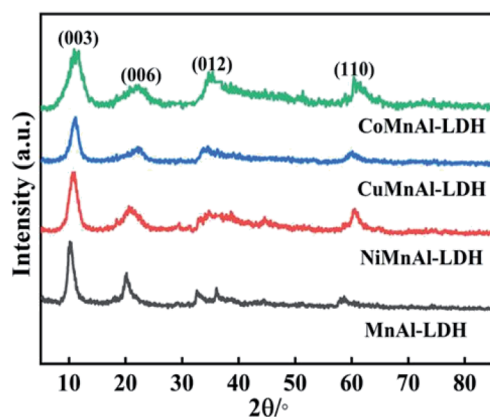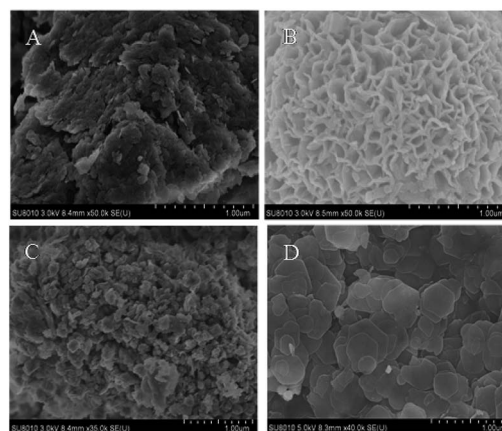

Fig. 2 SEM images of (A) MnAl-LDH, (B) CuMnAl-LDH, (C) NiMnAl-LDH and (D) CoMnAl-LDH.

dispersibility of the corresponding calcined products. This also can be certified by SEM and TEM characterization analysis.

3.1.2 SEM analysis. The morphologies of as-prepared LDHs were characterized using SEM. All samples presented brucite-like structure with well-defined platelets, as displayed in Fig. 2.

For unaltered MnAl-LDH, the agglomeration body was especially apparent, although there existed sheets on the surface of catalyst. After introducing the transition metal, the agglomeration was effectively improved. Surprisingly, the CoMnAl-LDH presented very thin and regular hexagonal platelets which were in favour of the gas–solid heterogeneous catalytic reactions.[21] For NiMnAl-LDH, the nanoplatelets were the same as CoMnAl-LDH, but the stacking was a little disordered. CuMnAl-LDH had similar "flower-like" shapes, consisting of very thick nanoplatelets.

3.1.3 FT-IR. The FT-IR spectra of MMnAl-LDHs are shown in Fig. 3. According to previous literature, the FT-IR spectra of all pristine LDHs deliver typical adsorption peaks like Mg–Al hydrotalcite.[22] It is clear that there exists a broad peak located at 3450 cm^{-1}, which can be assigned to the stretching vibrations

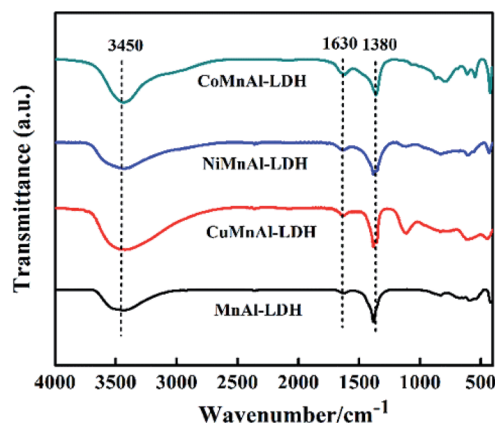Fig. 1 XRD patterns of MnAl-LDH, CuMnAl-LDH, NiMnAl-LDH and CoMnAl-LDH.

Fig. 3 FT-IR spectra of MnAl-LDH, CuMnAl-LDH, NiMnAl-LDH and CoMnAl-LDH.

of the –OH groups of the brucite-like layers.[23] All LDHs presented a similar peak located at 1630 cm^{-1} which can be assigned to the vibration of angular deformation of H_2O molecules.[24] The vibrations of CO_3^{2-} are related to the absorption band located at 1380 cm^{-1}.[25,26] Finally, the absorption bands in the range of 800–500 cm^{-1} can be ascribed to the vibrations of M–O from M–OH, O–M–O, or M–O–M in the hydrotalcite structure.[23–25] These data further suggest that LDH precursors were successfully synthesized.

3.2 SCR performance of the MMnAl mixed oxide catalysts

3.2.1 SCR activity. The Co-, Ni- or Cu-modified MnAl-LDO catalysts were obtained *via* calcination treatment at 500 °C to avoid the influence of residual organic fractions. The respective results of SCR activity and N_2 selectivity of MnAl-LDO, CoMnAl-LDO, NiMnAl-LDO and CuMnAl-LDO catalysts are presented in Fig. 4(A) and (B). It is worth mentioning that the different doping transition elements (Co, Ni, Cu) in the MnAl mixed oxides significantly influenced the catalytic performance. Notably, although the activity over the Ni-doped MnAl-LDO had a slight improvement in the low temperature region (<250 °C), the activity over Co-doped catalyst sharply rose, achieving 81% conversion of NO at 150 °C and above 95% conversion in the

range of 180 °C to 240 °C, much higher than the activity of the MnAl-LDO catalyst. However, another phenomenon can be observed during the process. After introduction of Cu into MnAl-LDO, the low-temperature activity (<250 °C) considerably decreased. Moreover, upon further increase of the temperature (>250 °C), the catalytic activity decreased dramatically for all catalysts. Fig. 4(B) shows the N_2 selectivity over all catalysts. Note that the MnAl catalyst presented worse N_2 selectivity than the Cu-, Co-, and Ni-doped catalysts in which the transition metals significantly enhanced the N_2 selectivity. As can be seen from the diagram, the sequence of transition metal enhancement of N_2 selectivity in the NH$_3$-SCR reaction system was ranked as follows: Ni > Co > Cu.

3.3 Structure–property correlation

3.3.1 XRD analysis of MMnAl mixed metal oxides. In Fig. 5, the XRD result displays the crystal phases of the MnAl-LDO, CuMnAl-LDO, NiMnAl-LDO, CoMnAl-LDO catalysts calcined at 500 °C. For MnAl-LDO samples, the diffraction pattern showed peaks at 18.1°, 28.9°, 30.7°, 32.5°, and 36.1°, corresponding to Mn_3O_4.[27] Meanwhile, the characteristic peaks assigned to CuO, NiO and Co_3O_4 were clearly observed in the respective CuMnAl-LDO, NiMnAl-LDO and CoMnAl-LDO catalysts.[21,28,29] In addition, except for the MnAl-LDO, there is no noticeable diffraction peak for MnO$_x$ observed in the XRD patterns of the Cu-, Co- and Ni-doped catalysts, indicating the good dispersion of MnO$_x$ on the catalyst surface.

3.3.2 BET analysis. For all catalysts, the N_2 adsorption–desorption isotherms are shown in Fig. 6. The isotherms presented a typical type IV isotherm accompanied by a type H$_2$ hysteresis loop, indicating capillary condensation occurring in a definite mesoporous structure.[30] It is clear that different doping transition metals affected the specific surface area to some degree, which may be related to the different calcined products from LDH precursors.[8] From this diagram, it can be found that the specific surface area of CuMnAl-LDO was slightly improved. In addition, the NiMnAl-LDO and CoMnAl-LDO catalysts were found to have higher surface areas relative to
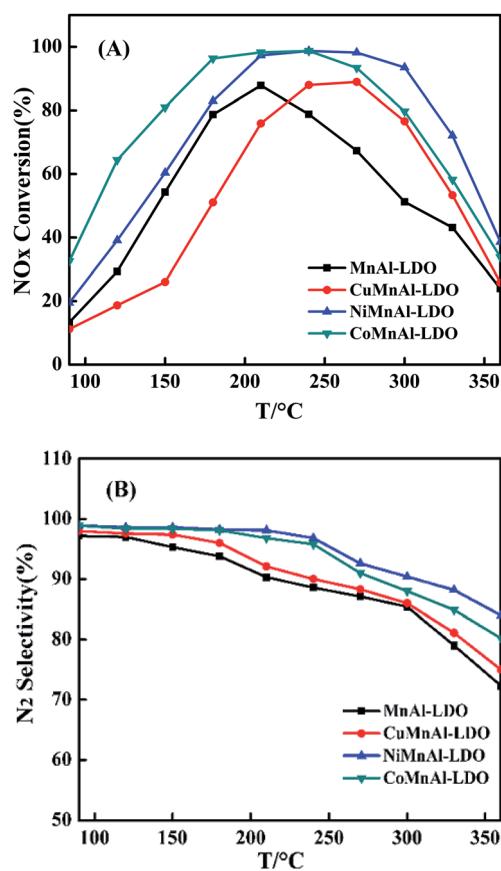

Fig. 4 (A) NO$_x$ conversion and (B) N_2 selectivity of MnAl–LDO, CuMnAl–LDO, NiMnAl–LDO and CoMnAl–LDO.
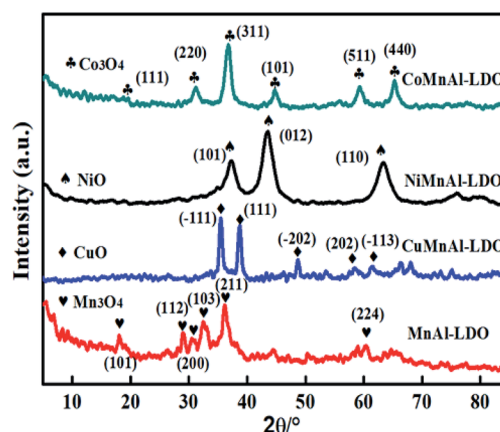

Fig. 5 The XRD patterns of MnAl–LDO, CuMnAl–LDO, NiMnAl–LDO and CoMnAl–LDO.
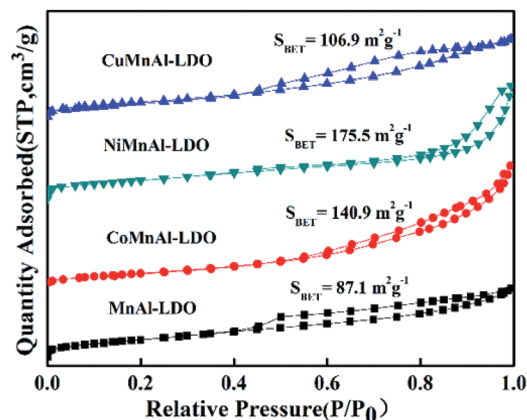
Fig. 6 The N_2 adsorption–desorption isotherms of MnAl-LDO, CuMnAl-LDO, NiMnAl-LDO and CoMnAl-LDO.

the MnAl-LDO and CuMnAl-LDO catalysts, and the two former possessed higher $DeNO_x$ activity. The result suggests that the higher surface areas are in favour of $DeNO_x$ activity because they
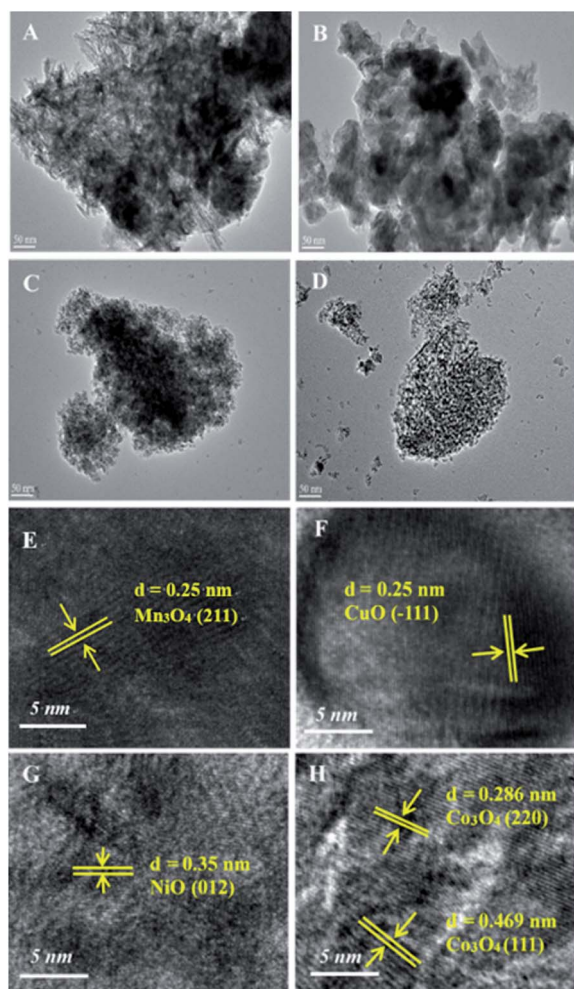
can offer more active sites for reactants.[31,32] An interesting phenomenon was discovered, in that NiMnAl-LDO displayed the largest specific surface area among all the catalysts while showing inferior catalytic performance to CoMnAl-LDO, hinting that the specific surface area is not the single influencing factor.

3.3.3   TEM analysis. The TEM analysis further disclosed the microstructures of the different mixed oxides, as shown in Fig. 7. For MnAl-LDO, the particles were clearly nonuniform in size and distribution and displayed apparent agglomeration. After introducing Cu, the above shortcomings were not much improved. Inspiringly, the nanoparticles were very uniformly distributed over the surface of CoMnAl-LDO and NiMnAl-LDO catalysts in comparison to the other two catalysts. For the MnAl-LDO catalyst, the obvious (211) crystal plane of Mn_3O_4 can be referenced to the lattice fringe of 0.25 nm.[33] The (−111) crystal plane of CuO and (012) crystal plane of NiO are found in Fig. 7(E) and (F) with lattice fringes of 0.25 nm and 0.35 nm,[21,34] respectively. The lattice fringes with interplanar distances of 0.28 nm and 0.46 nm can be respectively ascribed to the (220) and (111) planes of Co_3O_4.[35] These results further confirm the XRD results.

3.3.4   XPS analysis. In order to make clear the underlying causes, XPS spectra were acquired for MnAl-LDO and Cu-, Ni-, and Co-doped catalysts calcined at 500 °C, as illustrated in Fig. 8, with the relative concentration ratios summarized in Table 1. The XPS spectra of Mn 2p for all samples are shown in Fig. 8(A). After completing peak-fitting deconvolution for Mn $2p_{3/2}$, three distinct peaks at 642.0, 643.2, and 645.0 eV were observed, which can be correspondingly attributed to Mn^{3+}, Mn^{4+} and a satellite peak. Apparently, the amount of surface Mn^{4+} over the MnAl-LDO catalyst was higher compared with the other catalysts, which can result in excessive NH_3 oxidation at higher temperatures. Therefore, the MnAl-LDO catalyst afforded poor N_2 selectivity, as shown in Fig. 4(B). However, the Co and Ni additions endowed the CoMnAl-LDO and NiMnAl-LDO catalysts with reasonable oxidation through the full operating temperature range, which can give rise to not only improved low-temperature activity but also enhanced N_2 selectivity. Additionally, the Mn $2p_{3/2}$ peaks of the M-MnAl-LDO (M = Cu, Co, Ni) catalysts presented a minor shift toward lower binding energy compared to MnAl-LDO, indicating the existence of a strong interaction between MnO_x and MO_x, which would further make electron transfer more convenient.

Fig. 8(B) shows the XPS spectra of O 1s, which can be fitted into two characteristic peaks at 530.1 eV and 531.7 eV respectively belonging to lattice oxygen and chemisorbed oxygen, hereafter termed O_β and O_α. From Table 1, it can be clearly observed that the O_α/O_β ratio on the surface of the CoMnAl-LDO catalyst was higher than those of the other catalysts. The O_α, with higher mobility, is more conductive to oxidation reactions,[36] which can enhance the $DeNO_x$ activity of CoMnAl-LDO catalyst to some extent. Further XPS data processing revealed that Co^{3+}/Co^{2+}, Ni^{3+}/Ni^{2+} and Cu^{2+}/Cu^+ exist in the separate systems of CoMnAl-LDO, NiMnAl-LDO, CuMnAl-LDO. In general, more Co^{3+}, Ni^{3+} and Cu^{2+} species were preferable for redox ability, while the existence of redox circles like $Co^{3+} + Mn^{3+} \leftrightarrow Co^{2+} + Mn^{4+}$, $Ni^{3+} + Mn^{3+} \leftrightarrow Ni^{2+} + Mn^{4+}$ and $Cu^{2+} +$

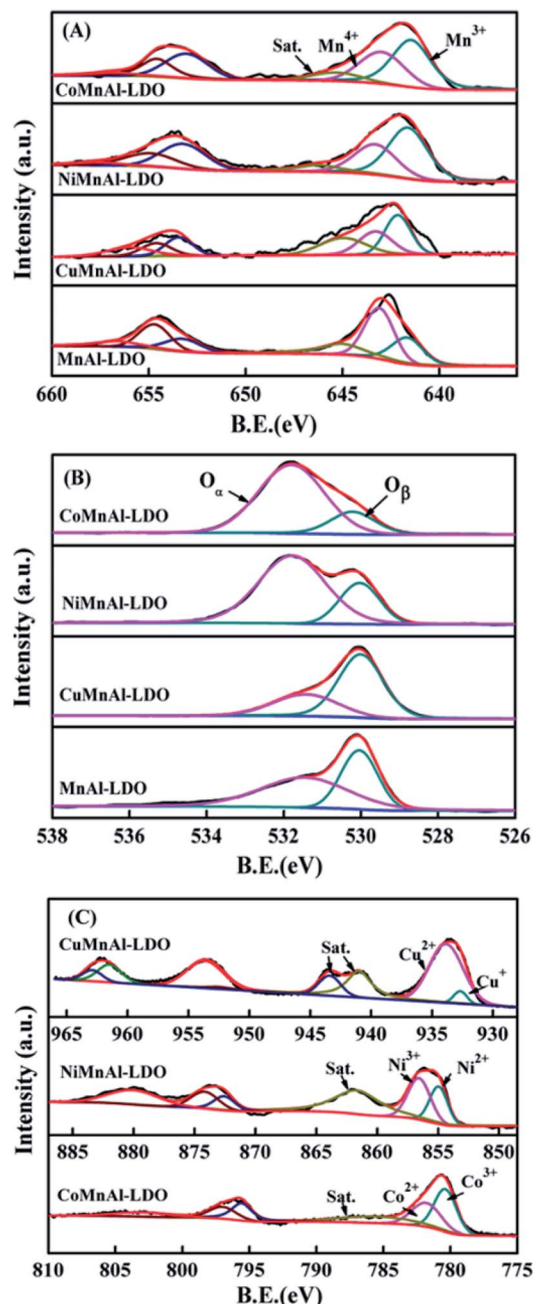Fig. 7   TEM images of (A and E) MnAl-LDO, (B and F) CuMnAl-LDO, (C and G) NiMnAl-LDO and (D and H) CoMnAl-LDO.

Fig. 8 XPS results of (A) Mn 2p, (B) O 1s, and (C) Cu 2p, Ni 2p, and Co 2p for MnAl-LDO, CuMnAl-LDO, NiMnAl-LDO and CoMnAl-LDO.

Table 1 Surface oxidation states calculated from XPS

Catalysts	Mn 2p Mn^{4+}/Mn^{3+}	O 1s O_{α}/O_{β}	Cu 2p Cu^{2+}/Cu^{+}	Ni 2p Ni^{3+}/Ni^{2+}	Co 2p Co^{3+}/Co^{2+}
MnAl-LDO	1.66	1.10	—	—	—
CuMnAl-LDO	0.62	0.68	12.04	—	—
NiMnAl-LDO	0.67	2.77	—	1.38	—
CoMnAl-LDO	0.75	3.70	—	—	1.47

peak in the temperature range of 300–400 °C in which Co_3O_4 and MnO_x were gradually reduced. Additionally, the peak in the high-temperature region (500–900 °C) could be assigned to the reduction of CoO or cobalt aluminates.[40] For NiMnAl-LDO catalyst, the reduction peak located at 489 °C corresponded to the reduction of Ni^{3+}/Ni^{2+} to NiO coupled with the reduction of amorphous MnO_x.[41] This result indicates that doping transition metals can change the redox ability of the MnAl-LDO catalyst. Among these metals, a more suitable interaction between CuO_x species and MnO_x may be responsible for the lower reducing temperature. As the number of reducible species on the surface of catalyst is also an important factor affecting the $DeNO_x$ activity, the hydrogen consumption for each catalyst was calculated and is shown in Table 2. Obviously, the CoMnAl-LDO (10.1 mmol g^{-1}) and NiMnAl-LDO (11.3 mmol g^{-1}) catalysts consumed more hydrogen than MnAl-LDO (6.4 mmol g^{-1}), indicating there were more reducible species over the surfaces of CoMnAl-LDO and NiMnAl-LDO which provide more redox sites and enable sufficient redox reactions. For the CuMnAl-LDO catalyst, the presence of a reduction peak at lower temperature can be an indication of its good reducibility. However, the limited redox sites (hydrogen consumption: 2.6 mmol g^{-1}) are a disadvantage which might account for its lower catalytic activity. The above results are, to some extent, in accordance with the catalytic performances of the catalysts.

3.3.6 NH₃-TPD analysis. NH_3-TPD measurements were used to study the number and strength of the acid sites over the

$Mn^{3+} \leftrightarrow Cu^+ + Mn^{4+}$ also played a major role in improving the catalytic activity.[37,38]

3.3.5 H₂-TPR analysis. The H_2-TPR technique was used to evaluate the surface redox behavior of the catalysts and the H_2-TPR profiles are shown in Fig. 9. For the pure MnAl-LDO catalyst, two reduction peaks observed at roughly 324 and 502 °C were assigned to the continuous reduction of $MnO_2/Mn_2O_3/Mn_3O_4 \rightarrow MnO$.[27] The TPR curve of CuMnAl-LDO catalyst shows a reduction peak at 284 °C which can be ascribed to the stepwise reduction of CuO, along with the reduction of MnO_x.[39] With regard to CoMnAl-LDO, there was a broad medium-temperature
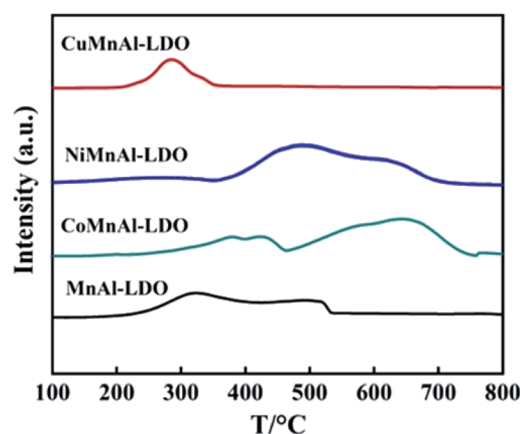

Fig. 9 H_2-TPR results of MnAl-LDO, CuMnAl-LDO, NiMnAl-LDO and CoMnAl-LDO.

Table 2 H_2 consumption and NO_x desorption of the four catalysts

Catalyst	Reduction temperature (°C)		H_2 consumption (mmol g^{-1})	NO_x desorption (%)			Total NO_x desorption (a.u.)
	T_1	T_2		100–150 °C	150–200 °C	>200 °C	
CoMnAl-LDO	395	646	10.1	38.9	31.7	29.4	2.5
NiMnAl-LDO	489	—	11.3	59.5	40.5	—	1.1
CuMnAl-LDO	284	—	2.6	—	42.9	57.1	1.3
MnAl-LDO	324	502	6.4	—	56.3	43.7	1

surface of the catalysts. As is well known, surface acidity is in favour of NH_3 adsorption, which is an essential step for the reaction in the NH_3-SCR system.[42] The NH_3-TPD profiles for all the catalysts are depicted in Fig. 10. The MnAl-LDO catalyst presented a small desorption peak at 143 °C belonging to the weak acid sites (<200 °C) and a large desorption peak at 303 °C belonging to the medium acid sites (200–450 °C). In contrast to MnAl-LDO catalyst, the weak acid sites of all transition-metal-doped catalysts increased significantly, suggesting that the addition of transition metals afforded more weak acid sites. Notably, although the weak acid sites of CuMnAl-LDO were improved, its ability for NO_x adsorption was weak, as confirmed in the NO + O_2-TPD analysis. The poor activity of CuMnAl in the low-temperature region can be further explained. It can also be seen that the strong acid sites, to a different extent, depend on the identity of the transition metal. Both NiMnAl-LDO and CoMnAl-LDO catalysts have a broad NH_3 desorption peak above 400 °C, which can be attributed to continuous NH_3 desorption on medium strong acid sites, while there were no strong acid sites on the surface of CuMnAl-LDO catalyst. These results demonstrated that strong acid sites were beneficial to NH_3 adsorption, proportional to the wide temperature windows of NiMnAl-LDO and CoMnAl-LDO catalysts.

3.3.7 NO + O_2-TPD analysis. As with the acid sites, the catalysts' adsorption behavior of the other major reactant (NO_x)

and its further activation also play an important role in the SCR reaction. Hence, NO + O_2-TPD for each catalyst was investigated and the results are shown in Fig. 11, with the *in situ* DRIFT spectra of NO + O_2 co-adsorption displayed in Fig. 12. The MnAl-LDO catalyst exhibits two desorption peaks located at 188 and 350 °C. After Cu modification, the number of NO_x adsorption sites slightly increased from 1 to 1.3 in CuMnAl-LDO, as shown in Table 2. However, it can be seen that the intensity of the desorption peak at low temperature (197 °C) decreased, while that of the high temperature desorption peak (352 °C) increased, implying the formation of more stable (normally more inactive) adsorbed NO_x species. This result can explain to a certain degree the inferior low temperature DeNO$_x$ activity of the CuMnAl-LDO catalyst. For the CoMnAl-LDO and NiMnAl-LDO catalysts, the desorption peaks were shifted to lower temperature region, indicating the Co- or Ni-doping can remarkably reduce the stability of the adsorbed NO_x species, which is more likely to provide reactive intermediates. Meanwhile, as can be seen in Table 2, doping with Co and Ni caused a new desorption peak below 150 °C, in which CoMnAl-LDO has a larger total desorption amount of NO_x than NiMnAl-LDO. These characteristics of CoMnAl-LDO could be associated with its superior low temperature DeNO$_x$ activity.

3.3.8 *In situ* DRIFT spectra. From the *in situ* DRIFT spectra (Fig. 12), the IR bands between 1620–1800 cm^{-1} can be ascribed
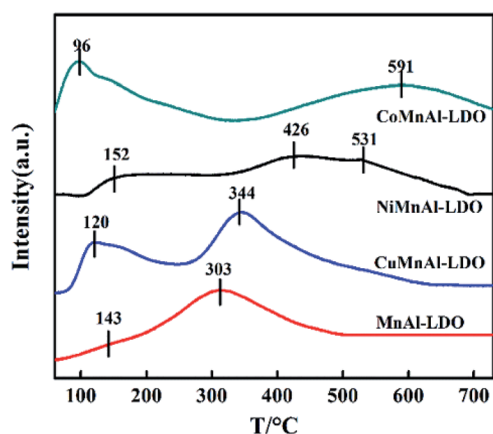

Fig. 10 NH_3-TPD results of MnAl-LDO, CuMnAl-LDO, NiMnAl-LDO and CoMnAl-LDO.
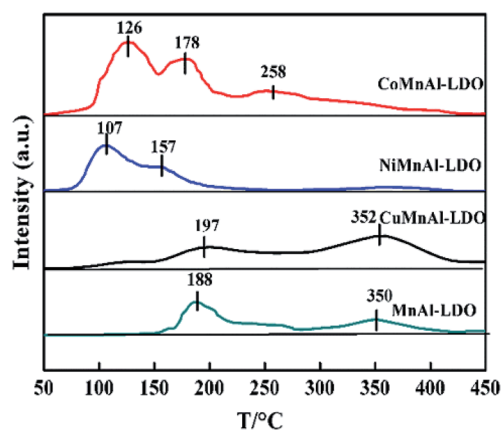

Fig. 11 NO + O_2-TPD results of MnAl-LDO, CuMnAl-LDO, NiMnAl-LDO and CoMnAl-LDO.
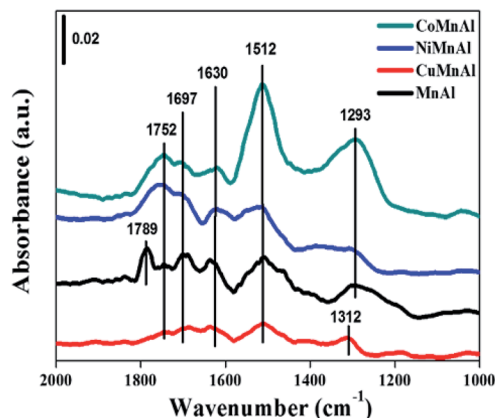
Fig. 12 *In situ* DRIFT spectra of NO + O$_2$ co-adsorption at 50 °C over MnAl-LDO, CuMnAl-LDO, NiMnAl-LDO and CoMnAl-LDO catalysts.

Fig. 13 Arrhenius plots of SCR reaction rates over MnAl-LDO, CuMnAl-LDO, NiMnAl-LDO and CoMnAl-LDO.

to physisorbed N$_x$O$_y$ molecules,[43] corresponding to the desorption peaks below 150 °C in Fig. 11. Generally speaking, weakly adsorbed NO$_x$ species can be easily activated to participate in the NH$_3$-SCR reaction and are beneficial to the improvement of DeNO$_x$ performance at low temperatures. In addition, the bands located at around 1512 cm^{-1} can be assigned to monodentate nitrate with relatively higher stability and can be related to the desorption peak between 150–200 °C. The desorption peaks at higher temperatures (>200 °C) can be attributed to more stable bidentate or bridged species, which are normally not as active as the monodentate species.[44] In summary, doping transition metals (Cu, Ni, Co) can affect the state of adsorption sites for NO$_x$ on the surface of MnAl-LDO catalysts to some extent. In comparison to CuMnAl-LDO and MnAl-LDO catalysts, CoMnAl-LDO and NiMnAl-LDO catalysts presented better low temperature catalytic activity based on their suitable NO$_x$ adsorption.

3.4 Kinetic analysis

3.4.1 Apparent activation energy. The calculation of apparent activation energy (E_a) can provide a valuable reference for evaluating the different catalytic activities. In the conventional NH$_3$-SCR reaction, the concentration of O$_2$ in the reactants is greatly excessive and NH$_3$ has a strong adsorption capacity. Thus, it is usually regarded as a quasi-first-order reaction (the reaction rate is first-order with respect to NO and zero-order with respect to NH$_3$) for kinetic evaluation.[45–49] Although this assumption may be imperfect, it can still provide a relatively valuable reference as a general way of calculating E_a in this study and the relevant formula for E_a has been presented in Section 2.4. It should be pointed out that the influences of internal and external diffusion have been excluded before calculating the apparent activation energy; corresponding experimental data are exhibited in Table S1, Fig. S1 and S2.† Fig. 13 shows the activation energy curves of the four catalysts at 90–210 °C; the E_a for MnAl-LDO, CuMnAl-LDO, NiMnAl-LDO, and CoMnAl-LDO were about 94.5 kJ mol^{-1}, 91.0 kJ mol^{-1}, 50.1 kJ mol^{-1}, and 45.8 kJ mol^{-1}, respectively. The results suggest that the removal of NO was accessible for NiMnAl-LDO
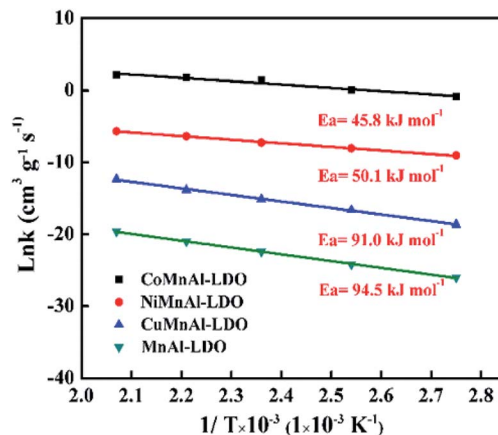
and CoMnAl-LDO and difficult for MnAl-LDO and CuMnAl-LDO catalysts, in agreement with the results of DeNO$_x$ activity. This result also indicates that the doping of MnAl-LDO by a transition metal (Co, Ni, Cu) can influence the activation energy of the reaction process to a certain extent, thereby promoting or inhibiting the NH$_3$-SCR reaction.

3.5 Stability test and H$_2$O/SO$_2$ resistance test

3.5.1 Stability test. To measure the duration of DeNO$_x$ activity for all the catalysts, a stability experiment was performed at 240 °C for 60 h under the same flue gas concentration adopted above, as shown in Fig. 14. After the test, the fluctuation value of DeNO$_x$ activity was 3.2% for the CoMnAl-LDO, which is slightly lower than that for NiMnAl-LDO (4%). For the CuMnAl-LDO and NiMnAl-LDO catalysts, the fluctuation values for the DeNO$_x$ activity were approximately 80%, much higher than that of CoMnAl-LDO. It is evident that the CoMnAl-LDO possesses a better stability.

3.5.2 H$_2$O/SO$_2$ resistance test. In practical use, residual fractions of SO$_2$ and H$_2$O will have some unpleasant side effects
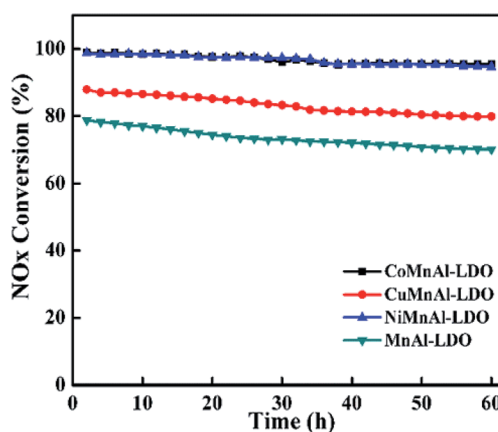

Fig. 14 The results of stability tests over MnAl-LDO, CuMnAl-LDO, NiMnAl-LDO and CoMnAl-LDO.
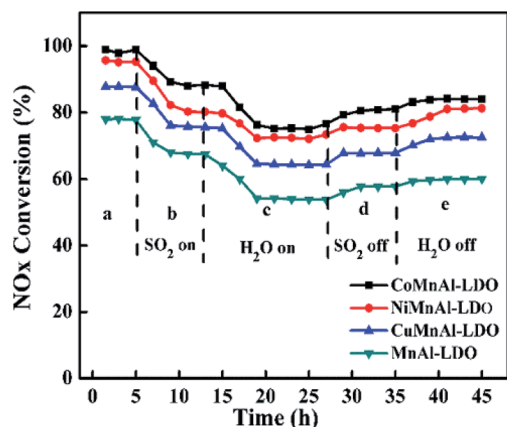
Fig. 15 The results of SO$_2$/H$_2$O durability over MnAl-LDO, CuMnAl-LDO, NiMnAl-LDO and CoMnAl-LDO.

the future potential for LDHs and provide a new mentality for heterogeneous catalysis.

Conflicts of interest

There are no conflicts of interest to declare.

Acknowledgements

on the elimination of NO$_x$ for all the catalysts. Therefore, the SO$_2$/H$_2$O durability as a function of time for all catalysts was tested in the NH$_3$-SCR reaction at 240 °C, as shown in Fig. 15. Initially, the NO$_x$ conversions were at 98.7%, 98.7%, 88.0%, and 78.8% for CoMnAl-LDO, NiMnAl-LDO, CuMnAl-LDO, and MnAl-LDO, respectively. When SO$_2$ was forced into the reaction system, all catalysts possessed lower DeNO$_x$ activity, declining to 88.3%, 80.2%, 75.6%, and 67.4% for CoMnAl-LDO, NiMnAl-LDO, CuMnAl-LDO, and MnAl-LDO, respectively. When both SO$_2$ and H$_2$O were inleted to the reaction system, a dramatic decrease occurred for all catalysts, especially for CuMnAl-LDO and MnAl-LDO with deceases as high as 23% and 25%. This suggests that there existed a synergistic inhibition effect on the NH$_3$-SCR reaction process due to the coexistence of SO$_2$ and H$_2$O. Previous reports have proved that the phenomenon is a result of the formation of sulfate particles that block pores and cover the catalyst surface.[50] When SO$_2$ was cut off, there were varied recoveries of DeNO$_x$ activity. When the supplies of both SO$_2$ and H$_2$O were closed, it was observed that the DeNO$_x$ abilities of CoMnAl-LDO and NiMnAl-LDO catalysts were restored to about 84% and 81.3%, while the DeNO$_x$ abilities for MnAl-LDO and CuMnAl-LDO were only restored to 60.1% and 72.5%, respectively. Thus, it can be deduced that the CoMnAl-LDO catalyst displayed excellent SO$_2$ and H$_2$O tolerance.

4.   Conclusions

In this study, a series of transition metal (Cu, Ni, Co) modified MnAl catalysts were obtained *via* calcining the corresponding LDH precursors and evaluated for the NH$_3$-SCR reaction. The obtained information suggested that the catalytic activities of the catalysts were strongly dependent on the identity of their transition metal, for which the NH$_3$-SCR reactivity order was CoMnAl-LDO > NiMnAl-LDO > CuMnAl-LDO. The fine catalytic performance in the broadest working temperature window over the CoMnAl-LDO catalyst should be attributed to its good dispersion of active species over the CoMnAl-LDO surface, which could contribute to its optimum redox behavior, plentiful acid sites and NO$_x$ adsorption sites. These findings might open

Notes and references

1 Z. Y. Fan, Z. Y. Wang, J. W. Shi, C. Gao, G. Gao, B. R. Wang, Y. Wang, X. Chen, C. He and C. M. Niu, *J. Catal.*, 2019, **370**, 30–37.

2 C. Fang, D. S. Zhang, L. Y. Shi, R. H. Gao, H. R. Li, L. P. Ye and J. P. Zhang, *Catal. Sci. Technol.*, 2013, **3**, 803–811.

3 U. Bentrup, A. Brückner, M. Richter and R. Fricke, *Appl. Catal., B*, 2001, **32**, 229–241.

4 J. Muñiz, G. Marbán and A. B. Fuertes, *Appl. Catal., B*, 2000, **27**, 27–36.

5 Z. Y. Fan, J. W. Shi, C. Gao, G. Gao, B. R. Wang, Y. Wang, C. He and C. M. Niu, *Chem. Eng. J.*, 2018, **348**, 820–830.

6 B. Thirupathi and P. G. Smirniotis, *J. Catal.*, 2012, **28**, 874–883.

7 S. Djerad, M. Crocoll, S. Kureti, L. Tifouti and W. Weisweiler, *Catal. Today*, 2006, **113**, 208–214.

8 B. H. Hou, Y. L. Du, X. Z. Liu, C. Ci, X. Wu and X. M. Xie, *RSC Adv.*, 2019, **9**, 24377–24385.

9 J. P. Dunn, P. R. Koppula, H. G. Stenger and I. E. Wachs, *Appl. Catal., B*, 1998, **19**, 103–117.

10 S. Andreoli, F. A. Deorsola, C. Galletti and R. Pirone, *Chem. Eng. J.*, 2015, **278**, 174–182.

11 X. L. Tang, J. M. Hao, W. G. Xu and J. H. Li, *Catal. Commun.*, 2007, **8**, 329–334.

12 F. Y. Gao, X. L. Tang, H. H. Yi, J. Y. Li, S. Z. Zhao, J. G. Wang, C. Chu and C. L. Li, *Chem. Eng. J.*, 2017, **317**, 20–31.

13 Z. H. Chen, Q. Yang, H. Li, X. H. Li, L. F. Wang and S. C. Tsang, *J. Catal.*, 2010, **276**, 56–65.

14 D. Fang, J. L. Xie, D. Mei, Y. M. Zhang, F. He, X. Q. Liu and Y. M. Li, *RSC Adv.*, 2014, **4**, 25540–25551.

15 M. Y. Qiu, S. H. Zhan, H. B. Yu, D. D. Zhu and S. Q. Wang, *Nanoscale*, 2015, **7**, 2568–2577.

16 H. Meng, J. N. Liu, Y. L. Du, B. H. Hou, X. Wu and X. M. Xie, *Catal. Commun.*, 2019, **119**, 101–105.

17 Y. K. Shao, J. H. Li, H. Z. Chang, Y. Peng and Y. X. Deng, *Catal. Sci. Technol.*, 2015, **5**, 3536–3544.

18 L. Chmielarz, P. Kuśtrowski, A. Rafalska-Łasocha, D. Majda and R. Dziembaj, *Appl. Catal., B*, 2002, **35**, 195–210.

19 Q. H. Yan, S. N. Chen, C. Zhang, D. O'Hare and Q. Wang, *J. Colloid Interface Sci.*, 2018, **526**, 63–74.

20 X. Wu, Y. L. Feng, X. Z. Liu, L. L. Liu, Y. L. Du and Z. Li, *Appl. Surf. Sci.*, 2019, **495**, 143513.

21 Q. H. Yan, Y. Nie, R. Y. Yang, Y. H. Cui, D. O'Hare and Q. Wang, *Appl. Catal., A*, 2017, **538**, 37–50.

22 C. Gennequin, T. Barakat, H. L. Tidahy, R. Cousin, J. F. Lamonier, A. Aboukaïs and S. Siffert, *Catal. Today*, 2010, **157**, 191–197.

23 J. M. Gatica and H. Vidal, *J. Hazard. Mater.*, 2010, **181**, 9–18.

24 C. J. Wang and D. O'Hare, *J. Mater. Chem.*, 2012, **22**, 23064–23070.

25 S. Kannan and V. Rives, *J. Solid State Chem.*, 2004, **177**, 319–331.

26 C. X. Yang, L. B. Liao, G. C. Lv, L. M. Wu, L. F. Mei and Z. H. Li, *J. Colloid Interface Sci.*, 2016, **479**, 115–120.

27 D. Zhao, C. Wang, F. Yu, Y. L. Shi, P. Cao, J. M. Dan, K. Chen, Y. Lv, X. H. Guo and B. Dai, *Nanomaterials*, 2018, **8**, 620.

28 X. J. Li, Y. L. Du, X. M. Guo, R. N. Wang, B. H. Hou and X. Wu, *Catal. Lett.*, 2018, **149**, 456–464.

29 X. Wu, Y. L. Feng, Y. L. Du, X. Z. Liu, C. L. Zou and Z. Li, *Appl. Surf. Sci.*, 2019, **495**, 14353.

30 S. P. Mo, S. D. Li, W. H. Li, J. Q. Li, J. Y. Chen and Y. F. Chen, *J. Mater. Chem. A*, 2016, **4**, 8113–8122.

31 Q. M. Jia, S. Y. Shan, L. H. Jiang, Y. M. Wang and D. Li, *J. Appl. Polym. Sci.*, 2012, **125**, 3560–3566.

32 F. D. Liu and H. He, *J. Phys. Chem. C*, 2010, **114**, 16929–16936.

33 S. N. Chen, Q. H. Yan, C. Zhang and Q. Wang, *Catal. Today*, 2019, **327**, 81–89.

34 Y. Nie, Q. H. Yan, S. Chen, D. O'Hare and Q. Wang, *Catal. Commun.*, 2017, **97**, 47–50.

35 B. Meng, Z. B. Zhao, X. Z. Wang, J. J. Liang and J. S. Qiu, *Appl. Catal., B*, 2013, **129**, 491–500.

36 X. Wu, Y. L. Feng, Y. L. Du, X. Z. Liu, C. L. Zou and Z. Li, *Appl. Surf. Sci.*, 2019, **467**, 802–810.

37 F. Y. Gao, X. L. Tang, H. H. Yi, S. Z. Zhao, J. G. Wang, Y. R. Shi and X. M. Meng, *Appl. Surf. Sci.*, 2018, **443**, 103–113.

38 H. Meng, J. N. Liu, Y. L. Du, B. H. Hou, X. Wu and X. M. Xie, *Catal. Commun.*, 2019, **119**, 101–105.

39 C. Z. Sun, J. Zhu, Y. Y. Lv, L. Qi, B. Liu, F. Gao, K. Q. Sun, L. Dong and Y. Chen, *Appl. Catal., B*, 2011, **103**, 206–220.

40 J. F. Lamonier, A. B. Boutoundou, C. Gennequin, M. J. Pérez-Zurita and S. Siffert, *Catal. Lett.*, 2007, **118**, 165–172.

41 S. X. Cai, D. S. Zhang, L. Y. Shi, J. Xu, L. Zhang, L. Huang, H. R. Li and J. P. Zhang, *Nanoscale*, 2014, **6**, 7346–7353.

42 X. Wu, H. Meng, Y. L. Du, J. N. Liu, B. H. Hou and X. M. Xie, *ACS Appl. Mater. Interfaces*, 2019, **11**, 32917–32927.

43 K. I. Hadjiivanov, *Catal. Rev.*, 2000, **42**, 71–144.

44 F. D. Liu, H. He, Y. Ding and C. B. Zhang, *Appl. Catal., B*, 2009, **93**, 194–204.

45 L. J. Yan, Y. Y. Liu, H. Hu, H. R. Li, L. Y. Shi and D. S. Zhang, *ChemCatChem*, 2016, **8**, 2267–2278.

46 S. C. Xiong, Y. Liao, X. Xiao, H. Dang and S. J. Yang, *J. Phys. Chem. C*, 2015, **119**, 4180–4187.

47 G. S. Qi and R. T. Yang, *J. Catal.*, 2003, **217**, 434–441.

48 G. S. Qi, R. T. Yang and R. Chang, *Appl. Catal., B*, 2004, **51**, 93–106.

49 R. H. Gao, D. S. Zhang, P. Maitarad, L. Y. Shi, T. Rungrotmongkol, H. R. Li, J. P. Zhang and W. G. Cao, *J. Phys. Chem. C*, 2013, **117**, 10502–10511.

50 X. N. Lu, C. Y. Song, S. H. Jia, Z. S. Tong, X. L. Tang and Y. X. Teng, *Chem. Eng. J.*, 2015, **260**, 776–784.